



FP-CNN: Fuzzy pooling-based convolutional neural network for lung ultrasound image classification with explainable AI



Md Mahmudul Hasan ^a, Muhammad Minoar Hossain ^{a,b}, Mohammad Motiur Rahman ^a, AKM Azad ^c, Salem A. Alyami ^c, Mohammad Ali Moni ^{d,e,*}

^a Department of Computer Science and Engineering, Mawlana Bhashani Science and Technology University, Tangail, 1902, Dhaka, Bangladesh

^b Department of Computer Science and Engineering, Bangladesh University, Mohammadpur, Dhaka, 1207, Bangladesh

^c Department of Mathematics and Statistics, Faculty of Science, Imam Mohammad Ibn Saud Islamic University (IMSIU), Riyadh, 13318, Saudi Arabia

^d Artificial Intelligence & Data Science, School of Health and Rehabilitation Sciences, The University of Queensland, Brisbane, QLD 4072, Australia

^e Artificial Intelligence and Cyber Futures Institute, Charles Stuart University, Bathurst, NSW 2795, Australia

ARTICLE INFO

Keywords:
COVID-19 diagnosis
Explainable artificial intelligence (XAI)
Fuzzy pooling
Ultrasound image classification

ABSTRACT

The COVID-19 pandemic wreaks havoc on healthcare systems all across the world. In pandemic scenarios like COVID-19, the applicability of diagnostic modalities is crucial in medical diagnosis, where non-invasive ultrasound imaging has the potential to be a useful biomarker. This research develops a computer-assisted intelligent methodology for ultrasound lung image classification by utilizing a fuzzy pooling-based convolutional neural network FP-CNN with underlying evidence of particular decisions. The fuzzy-pooling method finds better representative features for ultrasound image classification. The FPCNN model categorizes ultrasound images into one of three classes: covid, disease-free (normal), and pneumonia. Explanations of diagnostic decisions are crucial to ensure the fairness of an intelligent system. This research has used Shapley Additive Explanation (SHAP) to explain the prediction of the FP-CNN models. The prediction of the black-box model is illustrated using the SHAP explanation of the intermediate layers of the black-box model. To determine the most effective model, we have tested different state-of-the-art convolutional neural network architectures with various training strategies, including fine-tuned models, single-layer fuzzy pooling models, and fuzzy pooling at all pooling layers. Among different architectures, the Xception model with all pooling layers having fuzzy pooling achieves the best classification results of 97.2% accuracy. We hope our proposed method will be helpful for the clinical diagnosis of covid-19 from lung ultrasound (LUS) images.

1. Introduction

COVID-19 is a contagious illness occurred by the SARS-CoV-2 virus. This disease has triggered a pandemic worldwide from the year 2019 to 2022. Still, in 2023, the disease shows its strength by infecting people and causing deaths. Worldwide statistics show that till June 3, 2022, the disease has caused an overall 528,816,317 infections and 6,294,969 deaths. Fig. 1 shows these infectious cases region-wise [1].

The majority of the patients infected by the SARS-CoV-2 virus observe soft to endurable respiratory sickness and eventually recover it without taking any exceptional treatment. Although many patients demonstrate severe conditions and require special medical treatment, the ones with old age and other critical diseases are most susceptible

to this case. However, anybody may get infected by COVID-19 at any age and get critically ill or pass away. COVID-19 may spread by an affected person's tiny fluid particles from the nose or mouth. The ideal way to mitigate and confine the transmission of this disease is to identify the infected people and maintain social distance from them [2]. So, identifying COVID-19-infected people is an integral approach for mitigating the spread of the SARS-CoV-2 virus. Currently, reverse transcription polymerase chain reaction (RT-PCR) and antibody tests utilize most commonly for COVID-19 patient identification. These techniques require human interaction directly in some way to complete the action. Being an infectious disease, human interaction during testing is always a risky task. Moreover, RT-PCR and antibody tests cannot provide

* Corresponding author at: Artificial Intelligence & Data Science, School of Health and Rehabilitation Sciences, The University of Queensland, Brisbane, QLD 4072, Australia.

E-mail addresses: mahmodul.mbstu@gmail.com (M.M. Hasan), minoarhossain16005@gmail.com (M.M. Hossain), motiurcse@mbstu.ac.bd (M.M. Rahman), kazad@imamu.edu.sa (A. Azad), salyami@imamu.edu.sa (S.A. Alyami), m.monu@uq.edu.au (M.A. Moni).

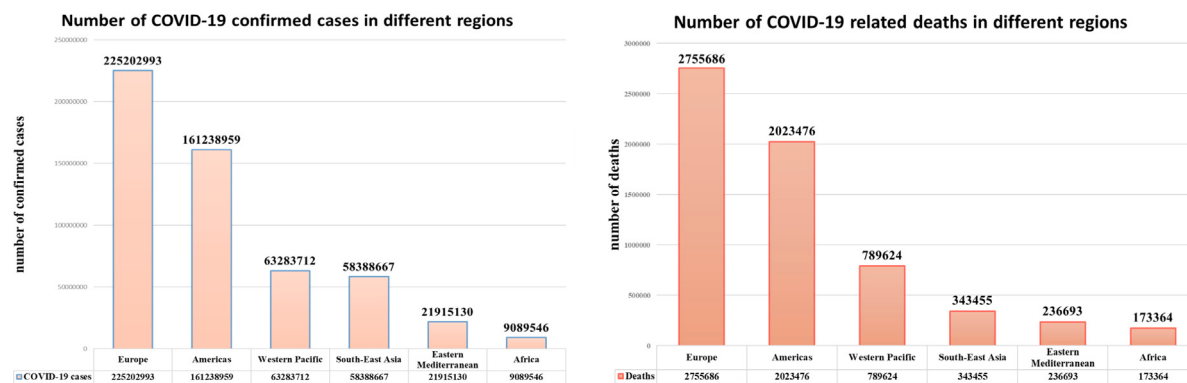


Fig. 1. The region-wise situation of COVID-19 cases. (Till June 23, 2022).

100% accuracy and setting up RT-PCR requires high cost [3,4]. Therefore, building up an automatic, secure, and cost-effective COVID-19 diagnosis scheme is a significant concern in health research.

In recent years, medical imaging-based AI methods like deep learning (DL) and machine learning (ML) techniques have been used in the health sector to build up automatic, secure, and cost-effective diagnosis schemes for many diseases such as tuberculosis, brain tumor, cancer, and others. For instance, authors in [5,6] have developed different DL-based strategies to identify tuberculosis from chest X-ray images. Studies including [7–9], the researchers present diverse, intelligent methods based on ML and DL to detect brain tumors from MRI images. These methods can automatically recognize any MRI image containing a tumor or other neurodegenerative diseases. Image segmentation-based methods have been playing a significant role in medical image processing by segmenting abnormal regions from images. Researchers in their studies [10–12] have proposed several segmentation methods for medical images of different types of disease diagnosis. Moreover, the following studies [13,14] have presented several DL-based methods to identify the different types of cancer from medical images. These methods can recognize a particular type of cancer from a specific medical image. So, such medical imaging-based artificial intelligence (AI) methods can be an effective solution to form the automatic and reliable COVID-19 scheme than the conventional RT-PCR and antibody tests. From this concern, researchers have generated and proposed several methods to detect COVID-19 from chest X-rays and CT scan images. For example, in studies including [15–19], the researchers present different methods based on ML and DL to identify COVID-19 patients from a chest X-rays image. From any input chest X-rays image, these methods can predict COVID-19 infection automatically. The researchers of these studies [20–22] have developed several automatic systems to predict a COVID-19-infected patient from a CT scan image. These ML and DL-based intelligent methods can detect any COVID-19 patient without the help of a medical expert [23,24]. Although many researchers use CT scans and X-ray images to build AI-based COVID-19 detection models, CT scans and X-ray possesses radiation exposure [25,26]. Consequently, ultrasound imaging has no radiation exposure and is the most cost-effective compared to X-ray and CT scans [27–30]. So, an ultrasound imaging-based intelligent method can be a feasible solution to generate reliable and automatic COVID-19 detection, which inspired to develop the research aim of this study, i.e., to develop an automated COVID-19 recognition system from ultrasound images.

This study uses a fuzzy-based pooling layer to construct a COVID-19 diagnosis approach from ultrasound images, and explainable AI (XAI) is used to explain the models' predictions. The SHAP library's gradient explainer is utilized to explain the predictions. We have experimented with five state-of-the-art CNN architectures and modified the pooling layers of the architectures with fuzzy pooling. In summary, our research has made significant contributions in the following areas:

- An intelligent fuzzy pooling-based convolution neural network for lung disease diagnosis methodology using lung ultrasound (LUS) images.
- The comparative analysis of different strategies, including without fuzzy pooling, single layer fuzzy pooling and all internal pooling layers using fuzzy pooling-based convolution neural network architectures.
- A thorough investigation of the reasons for models' predictions using explainable AI (XAI).

The rest of the paper consists of five ordered sections, e.g., Section 2 consists of the previous works on COVID-19 diagnosis using LUS images. Section 3 contains the proposed work's detailed techniques. The analysis and discussion of our study's findings are included in Section 4. The proposed method's performance metrics have also been compared to several existing research studies in that section. The discussion of our proposed method is in Section 5. Finally, Section 6 concludes the research and discusses future directions.

2. Related works

The prime concern of this research is to make a computerized automatic COVID-19 detection system from ultrasound images. To realize the current circumstance of this research, several existing research has been investigated and presented here. Diaz-Escobar et al. [31] developed a DL model, namely POCOVID-net, by modifying the VGG16 CNN architecture and including POCOVID-net they evaluated four other DL models, namely InceptionV3, Xception, VGG19, and ResNet50 to identify COVID-19 from lung ultrasound images (LUS) [32]. All of these models were evaluated in LUS images with three cases: (1) Detection of COVID-19, Pneumonia, and Healthy patient; (2) Detection of COVID-19 and Pneumonia patient; (3) Detection of COVID-19 and non-COVID19 patient. For these first, second, and third cases, the best accuracy gained were 89.1%, 94.1%, and 91.5%, respectively, by InceptionV3, POCOVID-net, and InceptionV3 models, respectively. All of these experiments were examined on a single LUS image dataset, which was substantially small-scale as mentioned by the authors as the core limitation of their work.

Born et al. [33] provided the first publicly available LUS dataset for COVID-19, namely the POCUS dataset. This dataset has drawn a significant focus of many researchers subsequently for building LUS imaging-based COVID-19 diagnosis systems. Besides providing the POCUS dataset, the authors also proposed a DL model developed by modifying the VGG16 CNN architecture, where the best accuracy that was achieved by this model was 89%. Later POCOVID-net was utilized by researchers of a study [31] to develop the LUS image-based COVID-19 diagnosis scheme. Muhammad and Hossain [34] developed a multilayer feature fusion-based CNN model to recognize COVID-19, Pneumonia, and Healthy patient from LUS images [35–38]. Their

proposed CNN model had five convolutional blocks where each block consisted of convolution connectors, and features were fused from these five blocks. The evaluation and experiment of their research showed that their CNN model provided better accuracy because of feature fusion. They also compared their CNN model with two well-recognized CNN techniques, namely ResNet50 and SqueezeNet, and found that their model was the best of these two models. The best accuracy of their model was 92.5%, whereas SqueezeNet, ResNet50, and their method without fusion gained 84.4%, 90.0%, and 86.6%, respectively. Barros et al. [39] suggested a hybrid DL model by combining CNN with Long short-term memory (LSTM) for recognizing COVID-19 from LUS images. They optimized the parameters of their proposed CNN-LSTM model by utilizing the Optuna framework. Different CNN models were evaluated for their hybrid CNN-LSTM model, and based on the outcome Xception model was selected to provide the best result of 93% accuracy.

To recognize COVID-19 by screening LUS images, Hou et al. [40] developed an interpretable subspace approximation model with an adjusted bias (Saab) multilayer network. This model was mainly designed to overcome the issue of iterative back-propagation of different intelligent networks like CNN. The authors claimed that the model was compatible with the portable device since the model did not require the large iterative back-propagation process, and gained an overall accuracy score of 96% for screening COVID-19 LUS images of A-line, B-line, and consolidation. Bhosale and Patnaik [41] developed an IoT-based DL mechanism to diagnose COVID-19 from chest X-rays. A lightweight DL model was developed in this research to execute through Raspberry Pi. The proposed research was able to recognize 7 lung diseases with 99.28% accuracy. To diagnose COVID-19 through IoT-empowered devices, Patnaik et al. [42] and Pal et al. [43] presented a customized DL model from a chest X-ray image. This model was capable of distinguishing between Pneumonia, COVID-19, and Normal patient, with an overall accuracy of 94.95%. Moreover, in their research [44], Bhosale and Patnaik presented a brief overview of the DL-based COVID-19 diagnosis, including challenges, opportunities, and applications of the DL mechanism for imaging-based COVID-19 diagnosis. The research could provide assistance while planning to design COVID-19 diagnosis research using imaging and the DL model. A study called PulDi-COVID developed a CNN technique to diagnose nine types of lung diseases, including COVID-19, from chest X-ray images [45] via an ensemble of different CNN models, and achieved an accuracy of 99.70%. Bhosale et al. presented a DenseNet169-based technique to classify nine categories of lung diseases, including COVID-19 [46], and diagnosed all of these diseases with an overall accuracy of 99.4%. Moreover, Bhosale et al. presented a capsule CNN and GNN-based approach to the diagnosis of COVID-19 and two other lung diseases from both CT scan and LUS images with an overall accuracy of 99.2% and 97.26% for CT scans and LUS images, respectively. In study [47], authors developed a DL mechanism for the diagnosis of COVID-19 from ECG images that attained an accuracy of 93.5% accuracy to classify cardiac and COVID-19 disease. Qi et al. proposed a segmentation method for COVID-19 X-ray images using a 2-dimensional histogram and 2D Kapur's entropy with nonlocal mean strategy [48]. Han et al. proposed a method by utilizing the Rosenbrock and diffusion mechanisms-based multilevel thresholding for COVID-19 chest X-ray segmentation [49].

All the above-mentioned methods discussed in this section, utilized common pooling techniques, namely max-pooling, min-pooling, and average-pooling. Note, these pooling techniques possess limitations to handle uncertainties that are generated during the convolution operation from the input layer to the hidden layers feature maps [50]. To overcome this limitation, here, in this research, we introduced a fuzzy pooling layer. Another limitation of existing methods was that they lack model explainability or performance explanation. To overcome this issue, in this research, we have introduced an explainable AI approach, namely XAI. Gunning et al. [51] and Doran et al. [52] mentioned Explainable Artificial Intelligence (XAI) as a set of actions and processes that assures end users to trust and perceive the outcomes produced by AI algorithms.

Table 1

Data distribution of train, test, and validation set (number of subjects with a number of images/frames).

Subject label	Train dataset	Validation dataset	Test dataset
Covid	23(934)	4(176)	6(243)
Pneumonia	24(989)	5(187)	8(259)
Normal	23(1002)	5(243)	6(272)

3. Methodology

This section explains the components of the suggested technique to diagnose lung infections such as COVID-19 using LUS images. Fig. 2 depicts a block schematic of the developed technique. The classification method is preceded by the image enhancement step, for which this study utilizes the isotropic diffusion for filtering, and then enhances the contrast of filtered images using the Contrast Limited Adaptive Histogram Equalization (CLAHE) method. Then, we trained our proposed fuzzy-pooling-based Xception network with enhanced images. The designed fuzzy-pooling-based CNN architecture works on the enhanced images to extract representative features for classification. Next, we have explained the outputs of black-box CNN models using the Gradient Explainer of the SHAP library.

3.1. Dataset description

The dataset is a collection of 166 LUS candidates of covid, bacterial pneumonia, and normal patients [33,53]. There are 134 short videos and 32 images of covid, pneumonia, and disease-free LUS images. The dataset is a collection of ultrasounds from multiple sources from different regions around the globe. In lung ultrasound collection, linear probe is more applicable, however, curved probes are widely used as ultrasound probes. The dataset contains images of both linear and curved probes, and the presence of both types of images helps to train the more robust model. The dataset is annotated by doctors and confirmed by performing RT-PCR tests for covid diagnosis [33]. This research only used bacterial pneumonia images from the dataset of [33]. The data of subjects are then divided into three groups using stratified random distribution: training (70%), testing (20%), and validation (10%). The stratified distribution maintains the original data distribution into sampling distributions. Table 1 shows the detailed information for the three sets described above. Next, the videos have been separated into image frames. Fig. 3 shows a few samples of ultrasound images from the training dataset. The dataset contains a total of 1353 COVID-19 images, 1435 disease-free images, and 1517 pneumonia images. Herein, we have used covid as shorthand for COVID-19 in this manuscript.

3.2. Image enhancement

Image enhancement is an effective processing step of our method. Noises, particularly speckle noise, are very common in ultrasound imaging. This research has applied image enhancement operations to reduce the artifacts. To enhance images, this work utilized contrast enhancement and spatial filtering techniques. We have applied Perona-Malik non-linear isotropic diffusion method as spatial filtering to reduce noises [54]. The spatial filtering technique avoids blurring and localization, which is critical for preserving image content such as edges. The filtering method usages the Eq. (1) where $|\nabla u|^2$ is the likelihood. Eq. (2) determines the diffusivity of the locations.

$$\partial_t(u) = \operatorname{div}(g(|\nabla u|^2) \nabla u) \quad (1)$$

The diffusivities of the locations using

$$g(s^2) = 1/(1 + (s/\lambda)^2), \text{ where } (\lambda > 0) \quad (2)$$

Contrast enhancement also has a significant role in image pre-processing tasks. However, immense change, in contrast, may remove

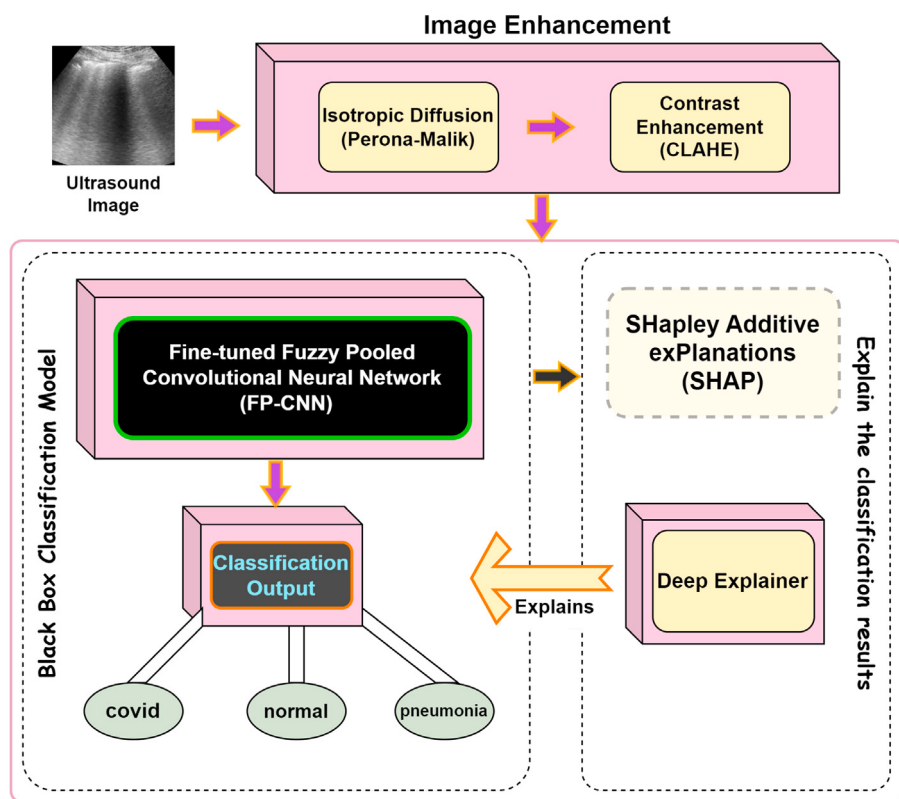


Fig. 2. The block diagram of the proposed method.

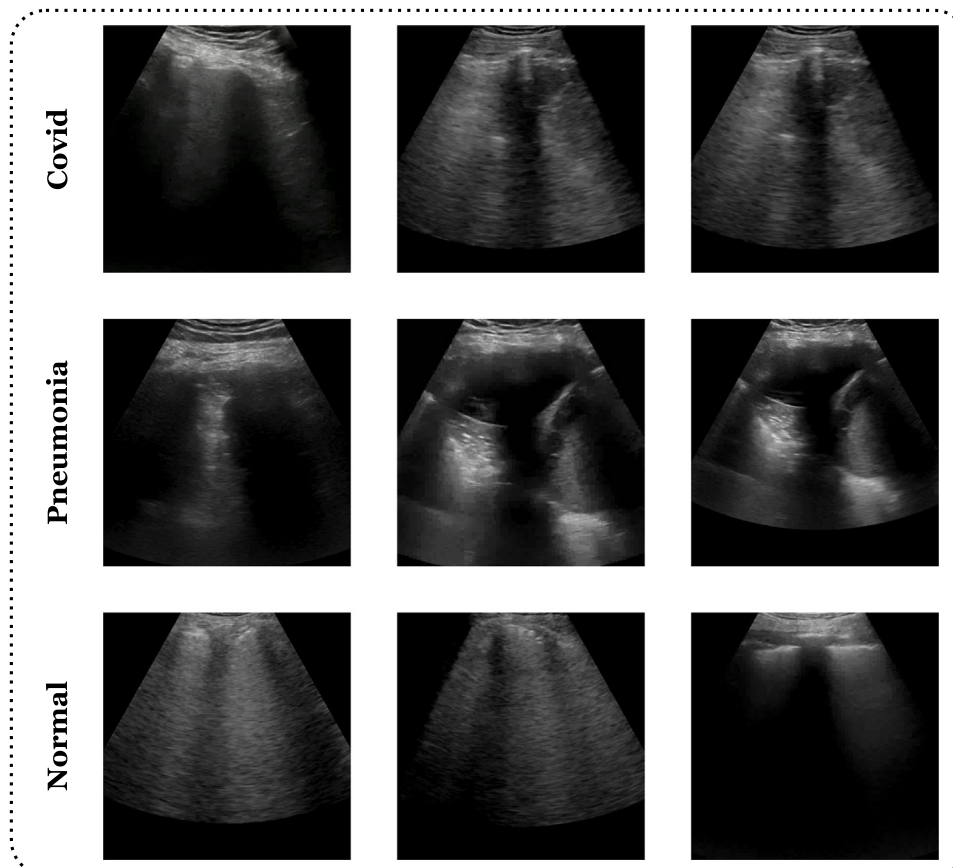


Fig. 3. Samples of covid, pneumonia, and disease-free (normal) images from the training dataset.

important features of an image. Our study has used Contrast Limited Adaptive Histogram Equalization (CLAHE) to enhance the contrast of the filtered images [55]. The CLAHE method operates on small spatial locations to perform contrast enhancement instead of the full image and interpolates the results of small spatial locations.

3.3. Fuzzy pooled convolutional neural network

The Convolution Neural Network (CNN) performs many operations to extract intuitive aspects from data to classify it. A CNN network can be broadly separated into two primary segments namely the convolution segment and the neural network segment. The convolution segment of the CNN itself may contain different forms of operations, such as convolution, activation, and pooling. The pooling operation is one of the most significant computations performed by CNN models. The pooling operation reduces the dimensions in height and width of the input feature map. The pooling processes that conduct the reduction operation include max-pooling, min-pooling, and average-pooling. Here in this study, we have made use of an efficient fuzzy-based pooling operation.

3.3.1. Fuzzy pooling

This study has utilized the fuzzy pooling operation in state-of-the-art CNN architectures. Fuzzy-based pooling method works in two steps as designed in [56]. In the first phase, the crisp value of the input is supplied to a fuzzy membership function. The fuzzified values are then reformed into crisp values using defuzzification. The inputs of a pooling layer are feature map that contains values within a range. In linguistic terms, those values can be classified as small, medium, or large. The feature maps that the pooling layer takes as input are the outputs of a convolution layer. The convolution layer performs convolution operations, and then the result goes through an activation function, specifically Rectified Linear Unit (ReLU). ReLU always gives non-negative values as output, which formulates the pooling layer's input feature map as a collection of non-negative values. The conversion of those non-negative values of the feature map into fuzzy values starts through the fuzzy membership functions. The value of $r_{max} = 6$ for the membership functions. This study uses three type-1 fuzzy membership functions (mf_v , where $v = 1, 2, 3$) to transform fuzzification as illustrated in Fig. 4. The function definitions are in Eqs. (3) to (5).

$$mf_1(FM_{i,j}^Z) = \begin{cases} 0 & FM_{i,j}^Z > d \\ \frac{d-FM_{i,j}^Z}{d-c} & c \leq FM_{i,j}^Z \leq d \\ 1 & FM_{i,j}^Z < c \end{cases} \quad (3)$$

where $d = \frac{r_{max}}{2}$ and $c = \frac{d}{3}$.

$$mf_2(FM_{i,j}^Z) = \begin{cases} 0 & FM_{i,j}^Z \leq a \\ \frac{FM_{i,j}^Z-a}{m-a} & a \leq FM_{i,j}^Z \leq m \\ \frac{b-FM_{i,j}^Z}{b-m} & m \leq FM_{i,j}^Z \leq b \\ 0 & FM_{i,j}^Z \geq b \end{cases} \quad (4)$$

where $a = \frac{r_{max}}{4}$, $m = \frac{r_{max}}{2}$ and $b = m + a$.

$$mf_3(FM_{i,j}^Z) = \begin{cases} 0 & FM_{i,j}^Z < r \\ \frac{FM_{i,j}^Z-r}{q-r} & r \leq FM_{i,j}^Z \leq q \\ 1 & FM_{i,j}^Z > q \end{cases} \quad (5)$$

where $r = \frac{r_{max}}{2}$ and $q = r + \frac{r_{max}}{4}$.

This study performs fuzzification on the feature map and gets three fuzzified versions of the feature map. Then we take patches of size

$k \times k$ from each fuzzified feature map (FFM) and aggregate the values of each patch, where k is a hyperparameter of the model. The aggregated value of each patch ($s_{\pi_v}^Z$) is the score of that patch to qualify for the overall membership of the patch (p^Z). Considering all the values of the ($s_{\pi_v}^Z$), a new value is selected for that patch (Eq. (6)). Eq. (7) selects the patches with high certainty. Fig. 5 illustrates the fuzzification steps of the pooling method. The fuzzification stage ends with this selection.

$$s_{\pi_v}^Z = \sum_{i=1}^k \sum_{j=1}^k \pi_{v,i,j}^Z \quad (6)$$

$$\pi' = \{\pi'_v | v = argmax(s_{\pi_v}^Z), Z = 1, 2, 3, \dots, z\} \quad (7)$$

The defuzzification stage reduces the dimensionality of patches. Here, in this study, we have used different defuzzification methods and found Center of Gravity (COG) as an effective technique Eq. (8). Fig. 6 visualizes the defuzzification of fuzzified values to crisp value representation for each patch. The network architecture of our method is — shown in Fig. 7.

$$p'^Z = \frac{\sum_{i=1}^k \sum_{j=1}^k (\pi'_{v,i,j} p_{i,j}^Z)}{\sum_{i=1}^k \sum_{j=1}^k \pi'_{v,i,j}} \quad (8)$$

where $p' = \{p'^Z | Z = 1, 2, 3, \dots, z\}$.

3.3.2. FP-CNN Architecture

This study tested five cutting-edge network designs, notably VGG16, VGG19, ResNet34, ResNet101, and Xception. We tested three distinct training procedures for classification. Section 4 displays the results of the examined models on various techniques. On performance metrics, the examined findings reveal that the Xception design with all internal pooling layers and fuzzy-based pooling is preferable. Fig. 7 presents the network architecture of our research. The global average pooling layer of the Xception architecture is not replaced by the fuzzy pooling layer in the architecture. We have altered all the internal max-pooling layers with fuzzy-based pooling layers. The fuzzy-pooling-based Xception model has 20,867,624 parameters in total among them 54,528 are non-trainable. VGG16 and VGG19 models have 15.5 million and 20.8 million trainable parameters. The ResNet34 model had 22.09 million parameters with 17,024 non-trainable parameters. ResNet101 had 45 million parameters and however, the model having 19 million trainable parameters gave the best results. All the models had two dense layers having 1024 and 256 neurons and a replaced global pooling layer before the first dense layer. We have used ReLU as an activation function for internal layers and softmax in the output layer. The kernel size of filters was 3×3 and stride was 2×2. The output layer (3 neurons) is connected with the global average pooling layer. Number of filters for all the layers entry flow (32, 64, 128, 128, 256, 256, 728, 728), middle flow (all layers had 728 filters), and exit flow (728, 1024, 1536, 2048) filters.

3.4. Explaining model prediction

The application of deep learning technology has grown tremendously over the decade. DL methods set new benchmarks for numerous tasks. Medical image analysis and disease diagnosis are substantial fields DL methods have been applied with a magical performance. However, the black-box approach of DL models hinders the flourishing of its practical implications. The undesirable biased DL models may fail in critical scenarios. For example, medical diagnosis requires shreds of evidence of why the model takes a particular decision. Thus, we need interpretable and explainable models to understand the reasons for its findings [57]. This study has worked with the eXplainable Artificial Intelligence (XAI) to explain the decision-making of the FP-CNN model.

Here, in this research, we have used the SHapley Additive exPlanations (SHAP) to explain the decisions of the black box FP-CNN model [58]. SHAP is a post hoc XAI method that uses feature relevance

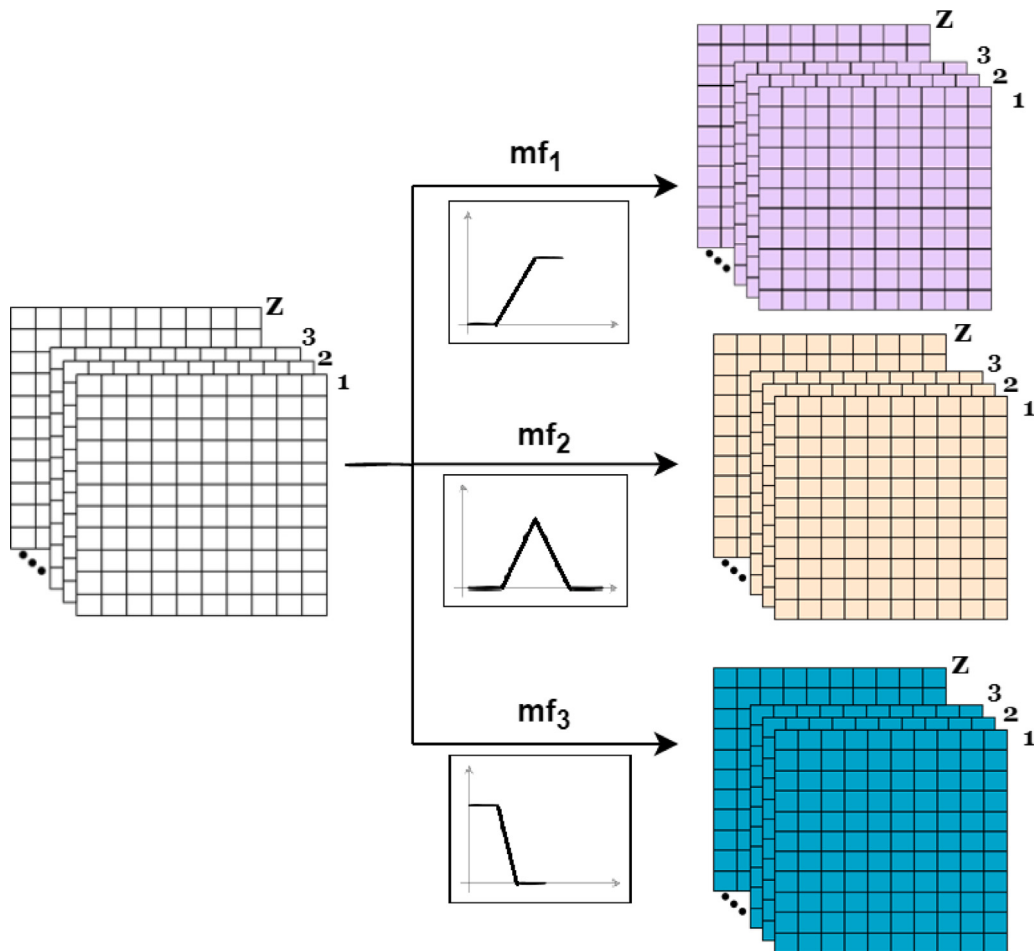


Fig. 4. The fuzzification of features map using three membership functions.

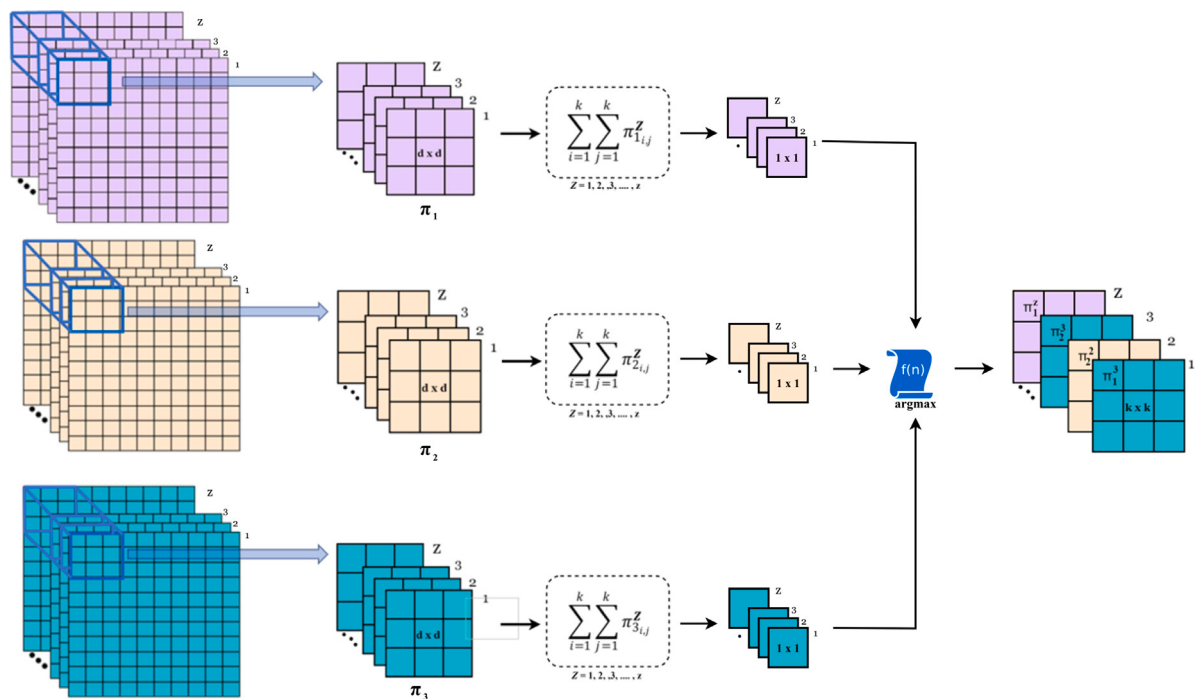


Fig. 5. The fuzzy pooling at each patch of size $k \times k$.

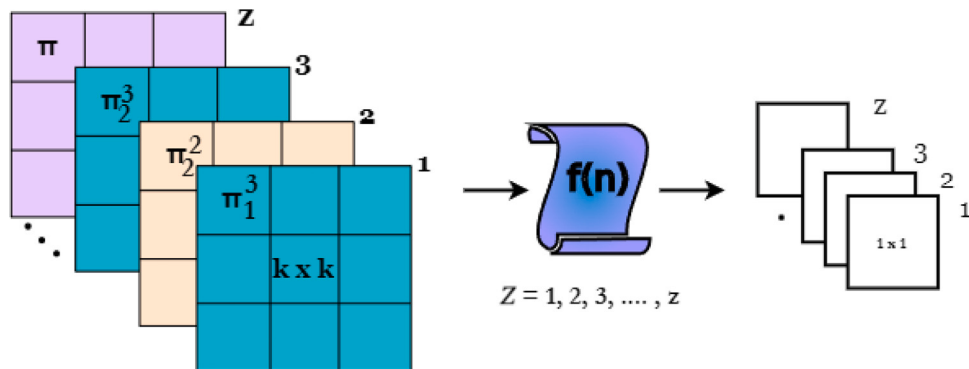


Fig. 6. The defuzzification of fuzzy values into crisp value.

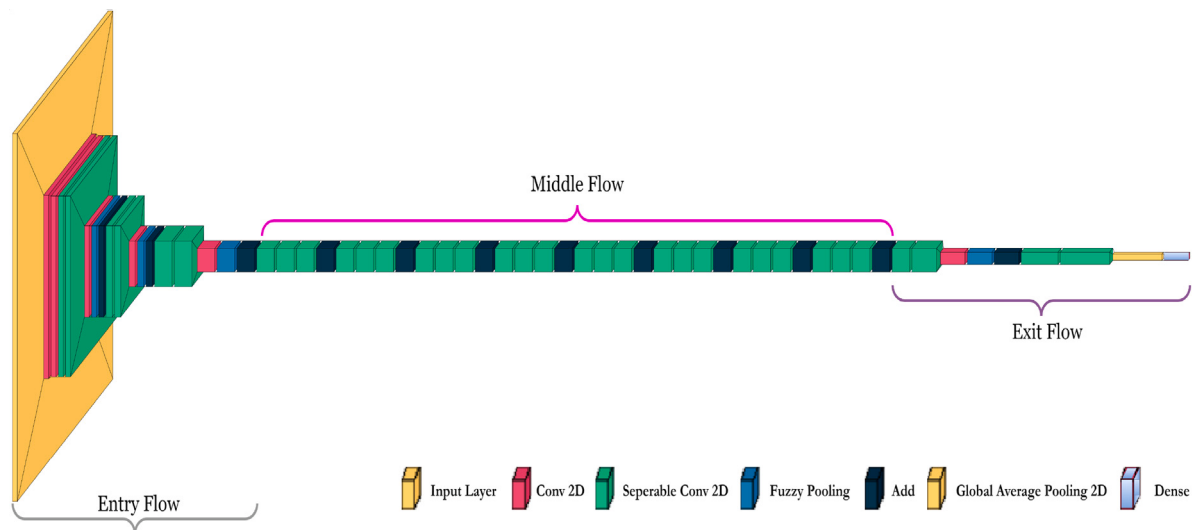


Fig. 7. The proposed FP-CNN architecture.

to provide an explanation. This study has utilized the gradient-based explanations to explain the effect of intermediate layers of the FP-CNN model on the predictions. The gradient explainer of SHAP uses the expected gradient technique to compute the integrated gradients over one or more paths between two valid inputs. SHAP computes the Shapley value of features by calculating the marginal contribution of features (ϕ_j). Eq. (9) computes the marginal contribution where $\hat{f}(x_{+j}^m)$ denotes the contribution of features with feature j and $\hat{f}(x_{-j}^m)$ defines the contribution of features without feature j.

$$\text{Marginal Contribution, } \phi_j^m = \hat{f}(x_{+j}^m) - \hat{f}(x_{-j}^m) \quad (9)$$

Shapley value of a feature is the average overall combinations ($\phi_j(x)$) for an example x (Eq. (10)).

$$\phi_j(x) = \frac{1}{M} \sum_{m=1}^M \phi_j^m \quad (10)$$

This study uses the SHAP library of [58] for explaining the outputs of the CNN model using a gradient explainer. The library provides the framework for explaining predictions of deep learning models. We have used the gradient explainer tool of the SHAP library to explain the deep learning models.

4. Performance analysis

This section contains the results of our research. The models are implemented in Python 3.7 on CPU - Core i7, RAM - 16 GB, GPU - Nvidia RTX 2070 Super Windows machine. The method was evaluated using

multiple performance metrics, specifically accuracy, recall, precision, specificity, Matthews correlation coefficient, and Cohen's kappa. We have implemented the network architecture in 'tensorflow-2.0' using Python as a language in jupyter notebook. Training the Xception model with fuzzy-pooling layers takes approximately 325 min and testing a single image takes 1.24 s. We have used 'visualkeras' library to draw the network architecture [59]. To compare our proposed strategy, we analyzed the performance of various models, including VGG16, VGG19, ResNet34, ResNet101, and Xception. The studies were carried out in three ways as described previously: fine-tuned models, single-layer fuzzy pooling on the architecture, and fine-tuning models by replacing all internal pooling layers with fuzzy pooling layers. We calculated the Matthews correlation coefficient for a single class and an overall test dataset. The single-class Matthews correlation coefficient is mentioned as the MCC score and for the entire test dataset, the Matthews correlation coefficient is abbreviated as the MCC score.

4.1. Performance metrics of fine-tuned models

The experiments modified the output layers of the SOTA architectures of the five models. The models have used the pre-trained weight of the 'ImageNet' dataset as the initial weight of fine-tuning with a meagre learning rate of $1e-4$. The training process continued until there was no improvement in the validation accuracy of the model for five epochs. Figs. 8 to 10 presents the performance of five fine-tuned models on each class of images. Fig. 8 shows the metrics of classification models on covid data. The ResNet101 and Xception had better results than other

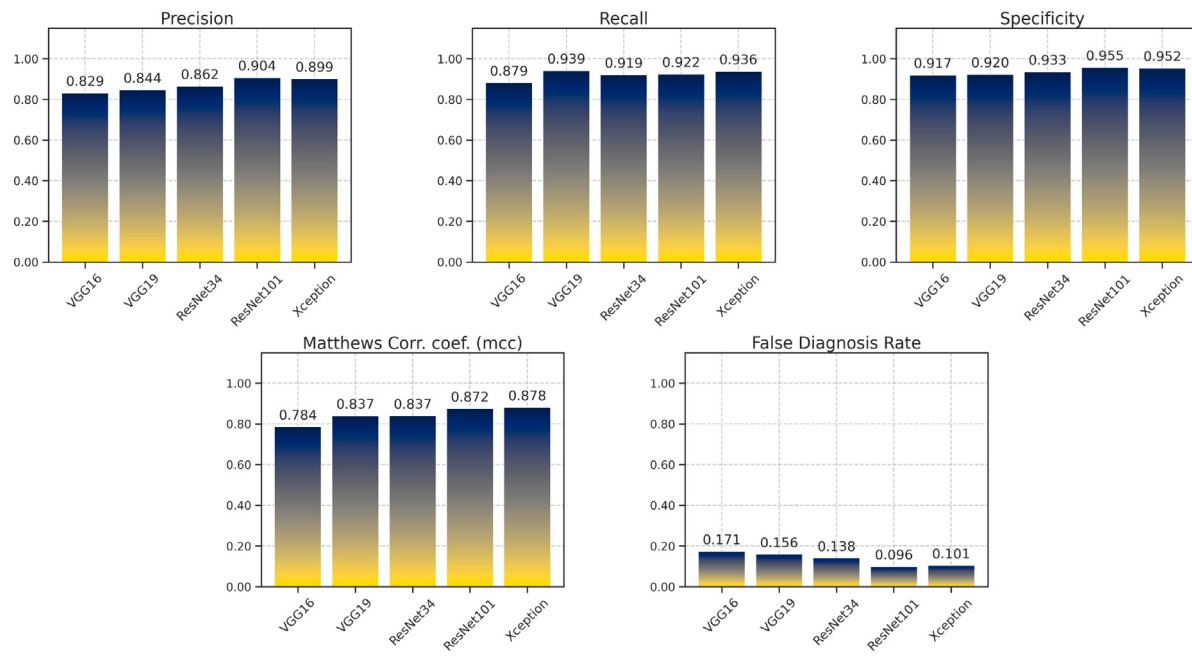


Fig. 8. Performance of different fine-tuned classifiers on covid data from the test dataset.

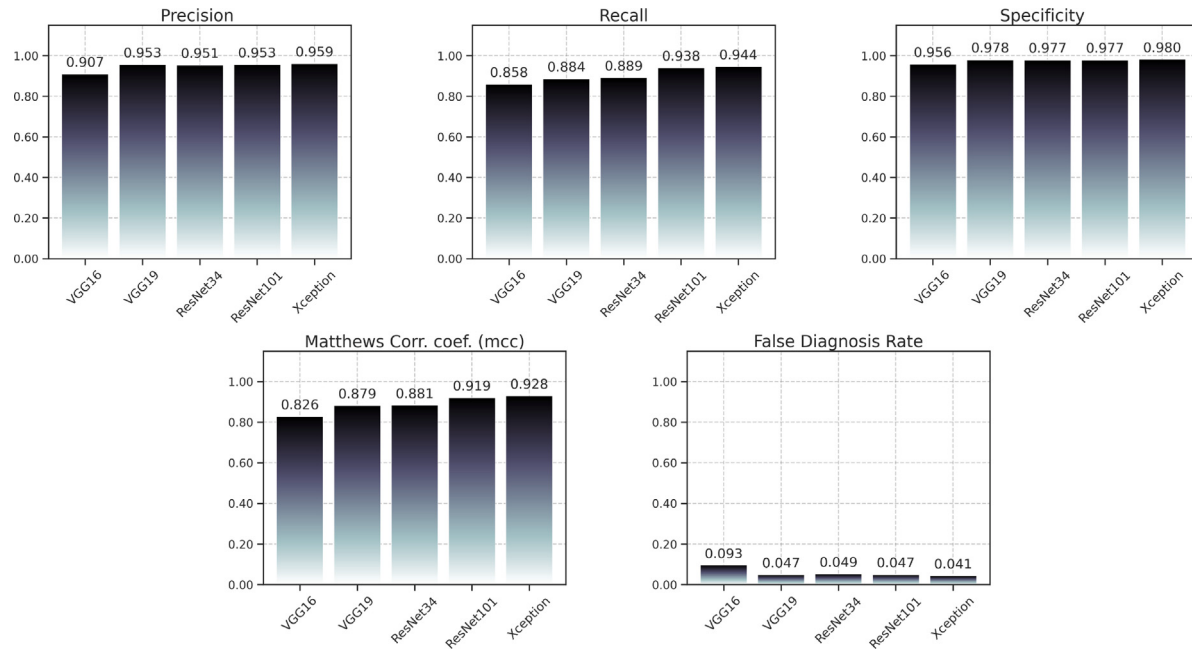


Fig. 9. Results of different fine-tuned classifiers on disease-free images from the test dataset.

models in identifying covid. The ResNet101 model achieved the best specificity, whereas Xception had the best recall and MCC score.

Fig. 9 shows the outcomes of fine-tuning models for disease-free ultrasound images. The precision, MCC, and FDR had the best values for the Xception net on disease-free images. The VGG16 had the least scores on each metric of disease-free images. The specificity scores of the classifiers were very close for each model. The metrics on pneumonia data are shown in Fig. 10. On pneumonia images, classifiers had the lowest MCC score. In every metric, the Xception model outperformed its competitors.

Fig. 11 shows the overall performance metrics of fine-tuned models. The model's overall performance was assessed using various criteria,

including accuracy, MCC, and Cohen's kappa. Xception did significantly better than other classifiers on the test dataset, with an accuracy of 0.931 and 0.896, for MCC and Cohen's kappa scores, respectively.

4.2. Performance metrics of single layer fuzzy pooled models

The selected models have a different number of pooling layers in their architecture. Thus, this research experimented with a different number of fuzzy pooling layers. This subsection presents the significance of fuzzy pooling by replacing the last pooling layer of each model with a fuzzy pooling layer. The experimented results are in Figs. 12 to 14. The outcome of fuzzy pooling was slightly better than

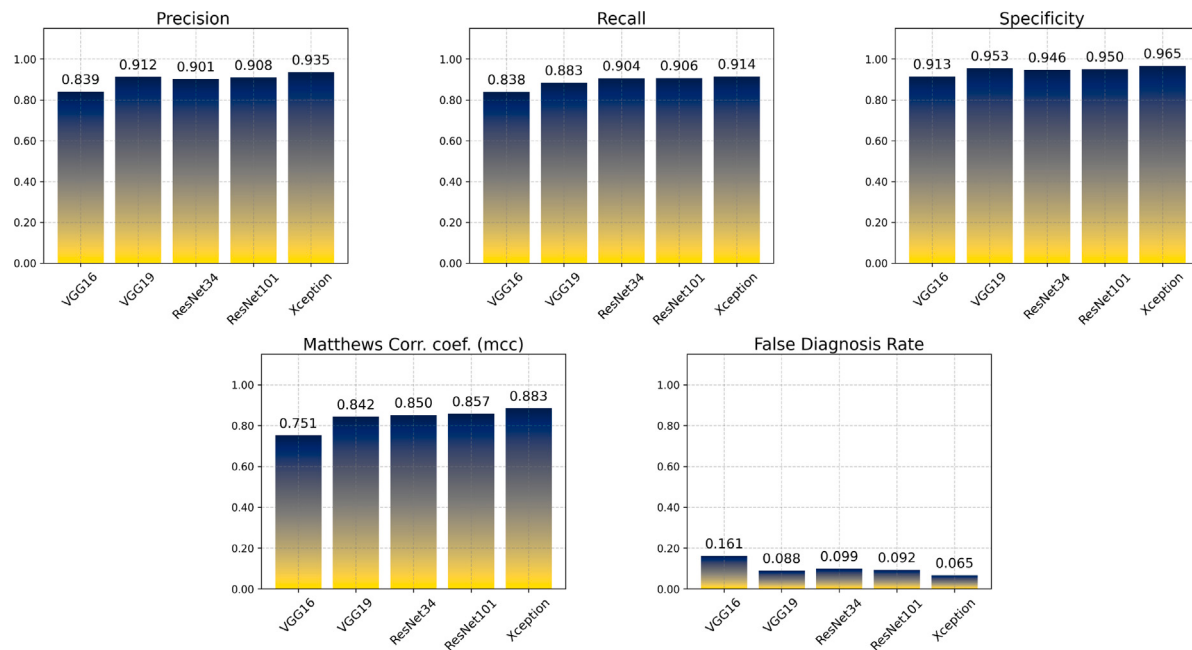


Fig. 10. Performance of different fine-tuned classifiers on pneumonia data from the test dataset.

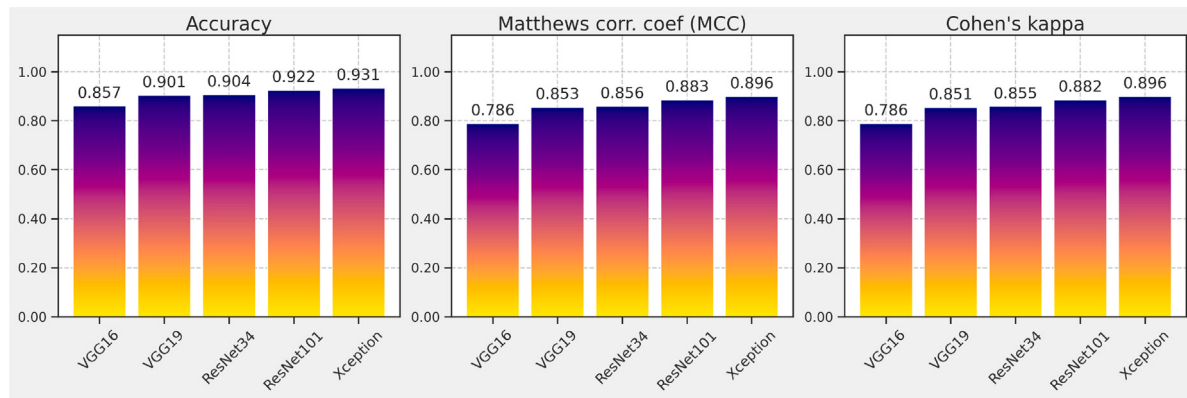


Fig. 11. Results of different fine-tuned classifiers on the entire test dataset.

models without fuzzy pooling. Fig. 11 shows the metrics of single-layer fuzzy pooled (SLFP) models on covid data. Each model achieved better values compared to the bars in Fig. 8. The Xception model attained more satisfactory results than other models in all five metrics, with 0.932 precision, 0.936 recall, 0.968 specificities, 0.904 MCC, and 0.068 FDR.

The bars of Fig. 13 present the metrics of SLFP models on normal data of the test dataset. The metrics were improved compared to previous metrics in Fig. 9. All the models had significant improvement in specificity scores, which indicates that models have learned better to differentiate disease-free samples. Fig. 14 illustrates the performance of SLFP models on pneumonia data. Here, the Xception model had better metrics in pneumonia detection. In addition, the models had enhanced performance scores compared to models without a fuzzy pooling layer.

Fig. 15 presents the performance metrics of SLFP models on the entire test set. The Xception had the best results in overall metrics with 0.953 accuracy and 0.929 of MCC and Cohen's kappa score. Compared to the previous results in Fig. 10, the Xception model increased the accuracy score by 0.022, the MCC score by 0.033, and Cohen's kappa score by 0.033. The highest dispersion was for the VGG16 model, with a 0.031 increase in accuracy and 0.046 in MCC and Cohen's kappa. The slightest improvement in metrics was observed for the VGG19 model.

4.3. Performance evaluation of models by replacing all pooling layers using Fuzzy-based pooling layer

This sub-section discourses the results of the SOTA architectures having fuzzy-based pooling in all of the pooling layers. We have used the pre-trained weights of the imangenet dataset to initialize weights of the network architectures and trained the model with a learning rate of $1e-4$ with an early stopping mechanism. Table 2 shows the classification metrics of models with fuzzy pooling. There was significant performance improvement for all the models except ResNet34 on covid data. The MCC score of ResNet34 was reduced compared to single-layer fuzzy pooling. Once again Xception model yielded the best results for covid data classification with better scores than previous bars of Figs. 8 and 12.

Table 3 presents the performances of normal data of the test dataset. The lowest false diagnosis error rate of disease-free normal data classification was 0.020 using the Xception model. Compared to other models, there was a significant improvement in all the metrics for the VGG16 and VGG19 models. There are more pooling layers in VGG nets compared to other models that extracted better features for classification.

Table 4 shows the performance metrics of pneumonia data. We have again seen similar characteristics of the models for pneumonia data

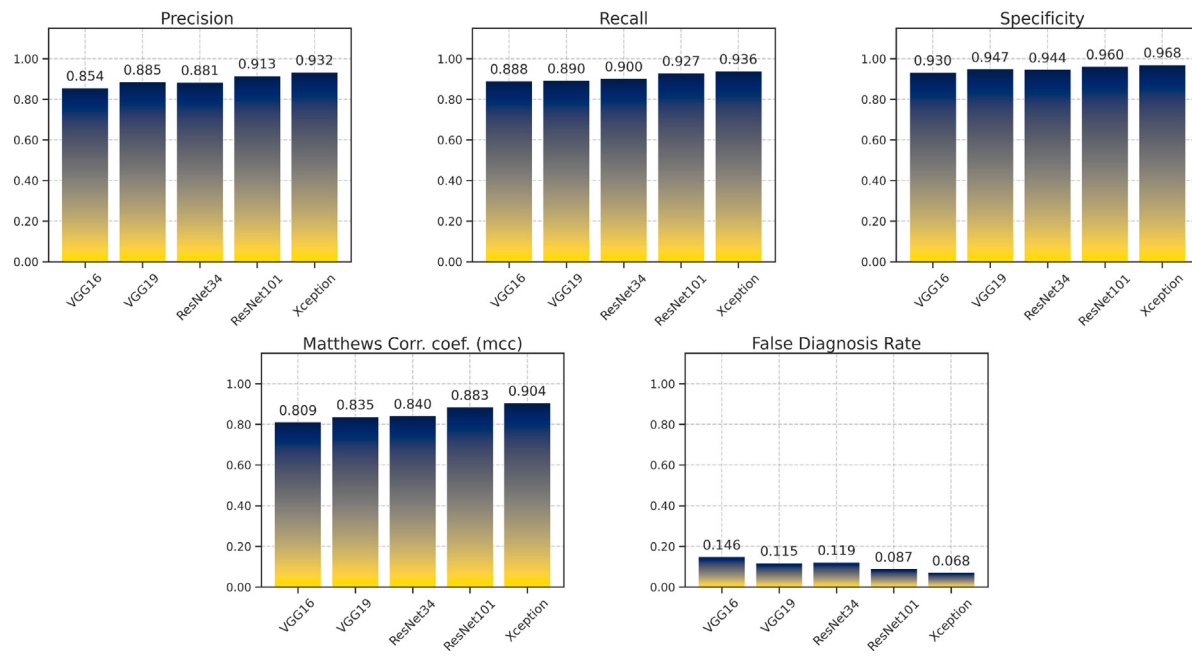


Fig. 12. Performance of different single-layer fuzzy classifiers on covid data.

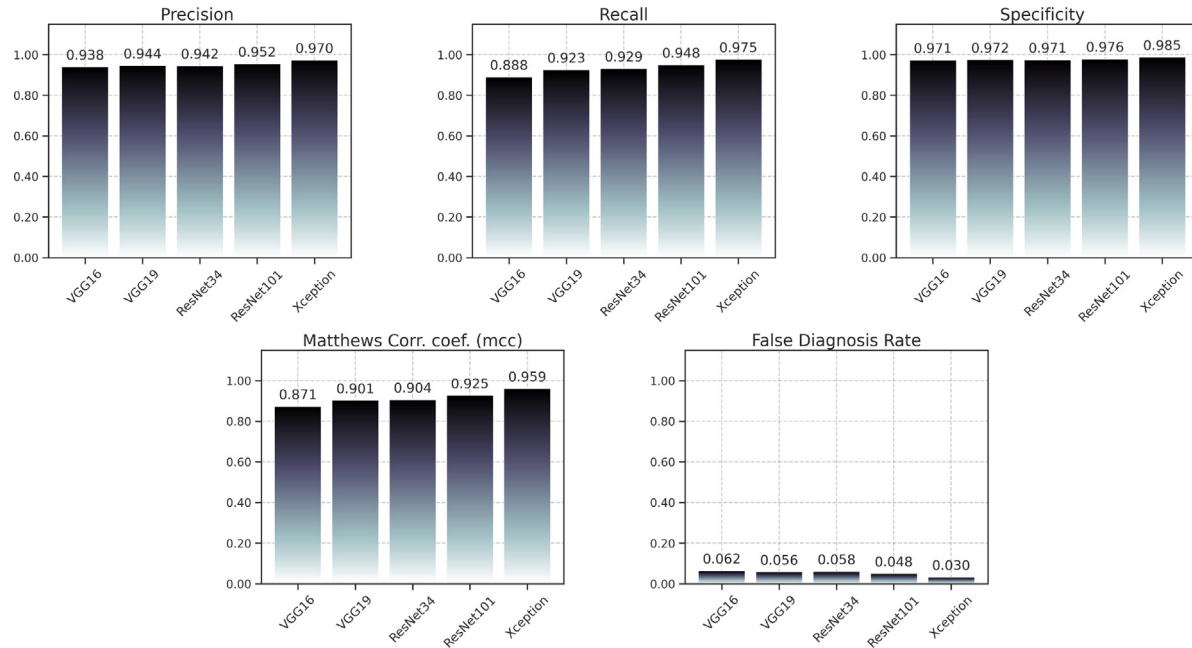


Fig. 13. Performance of different single-layer fuzzy pooling classifiers on disease-free images of the test dataset.

Table 2

Results of all fuzzy pooling layer-based classifiers on covid data.

	Precision	Recall	Specificity	MCC	FDR
VGG16	0.95349	0.94650	0.95669	0.89361	0.09091
VGG19	0.93117	0.95041	0.96798	0.91337	0.06883
ResNet34	0.89388	0.90123	0.95104	0.85039	0.10612
ResNet101	0.91870	0.93004	0.96234	0.88943	0.08130
Xception	0.96296	0.96296	0.98305	0.94601	0.03704

classification. The lowest MCC score was for the ResNet34 model, while the MCC score of VGG nets has improved significantly. The least FDR was observed for the Xception model and the highest one was observed for the ResNet34 model. Table 5 illustrates the overall performance

Table 3

Performance of all fuzzy pooling layer-based classifiers on disease-free images of the test dataset.

	Precision	Recall	Specificity	MCC	FDR
VGG16	0.96382	0.93822	0.97670	0.91851	0.04706
VGG19	0.96109	0.95367	0.98054	0.93602	0.03891
ResNet34	0.94163	0.93436	0.97087	0.90699	0.05837
ResNet101	0.95720	0.94981	0.97864	0.93025	0.04280
Xception	0.97701	0.98456	0.98835	0.97106	0.02299

metrics on the comprehensive test dataset. Note, the Xception model had the highest accuracy of 0.97157, Cohen's kappa of 0.95733, and an MCC score of 0.95732.

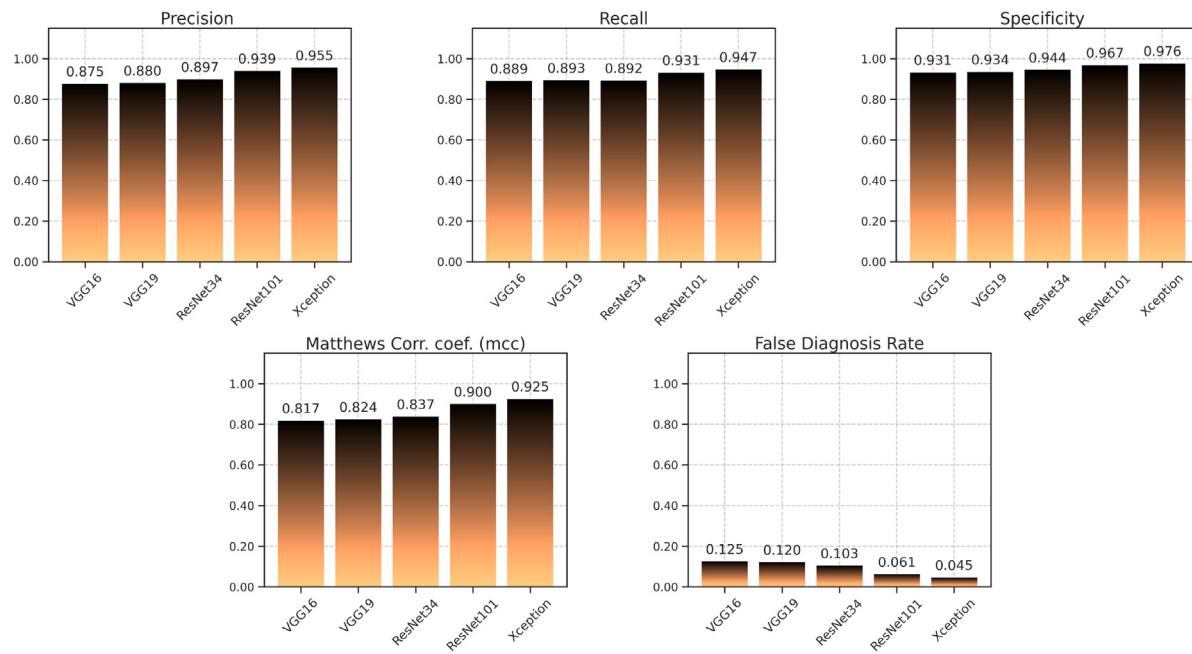


Fig. 14. Performance of different single-layer fuzzy pooling classifiers on pneumonia data.

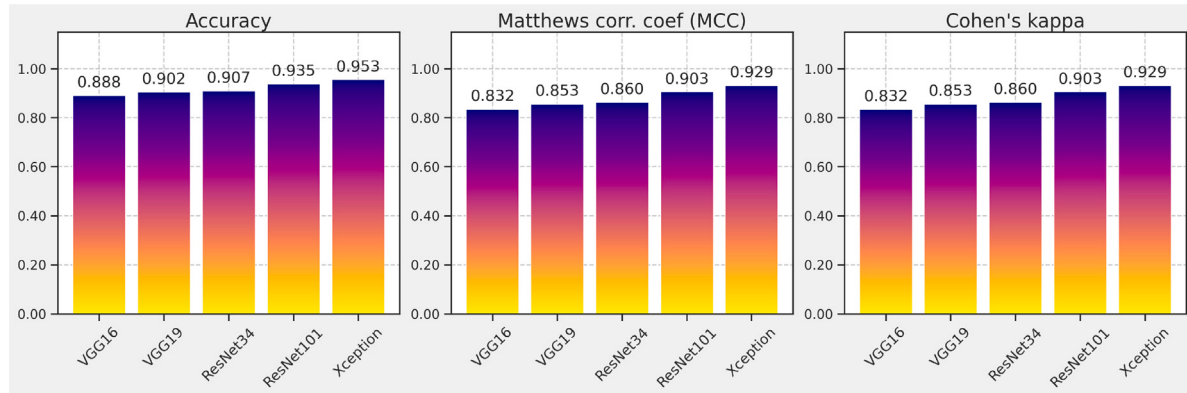


Fig. 15. Results of different single-layer fuzzy pooling classifiers on the test dataset.

Table 4
Results of all fuzzy pooling layer-based classifiers on pneumonia data.

	Precision	Recall	Specificity	MCC	FDR
VGG16	0.94832	0.91544	0.96614	0.88618	0.06391
VGG19	0.94796	0.93750	0.97206	0.91189	0.05204
ResNet34	0.90074	0.90074	0.94622	0.84695	0.09926
ResNet101	0.94096	0.93750	0.96813	0.90639	0.05904
Xception	0.97407	0.96691	0.98606	0.95459	0.02593

Table 5
Performance of all fuzzy pooling layer-based classifiers on the entire test dataset.

	Accuracy	MCC	Cohen's kappa score
VGG16	0.93281	0.89934	0.89917
VGG19	0.94695	0.92041	0.92037
ResNet34	0.91214	0.86809	0.86808
ResNet101	0.93927	0.90884	0.90883
Xception	0.97157	0.95733	0.95732

Analyzing different strategies, we have found the best results were observed from all layers with the fuzzy pooling-based Xception model. The Xception model did well in overall performance and single-class image classification. Fig. 16 depicts the analysis summary for a comparative understanding of classification methods. This research also evaluated the performance of our proposed method using five-fold cross-validation. The five-fold cross-validation results are illustrated in Fig. 17. The violin chart of Fig. 17 shows the precision, recall, specificity, and MCC score of covid, normal, and pneumonia images of each fold with deviation from the mean. Table 6 presents the comparison of accuracy with related studies in the literature. Our proposed method has the highest accuracy among compared recent studies on disease diagnosis in LUS images.

4.4. Explaining predictions

The gradient explainer of SHAP presents the contribution of each pixel for the prediction. Fig. 18 depicted the contribution map of each pixel on prediction. For visualizations, we choose the top two

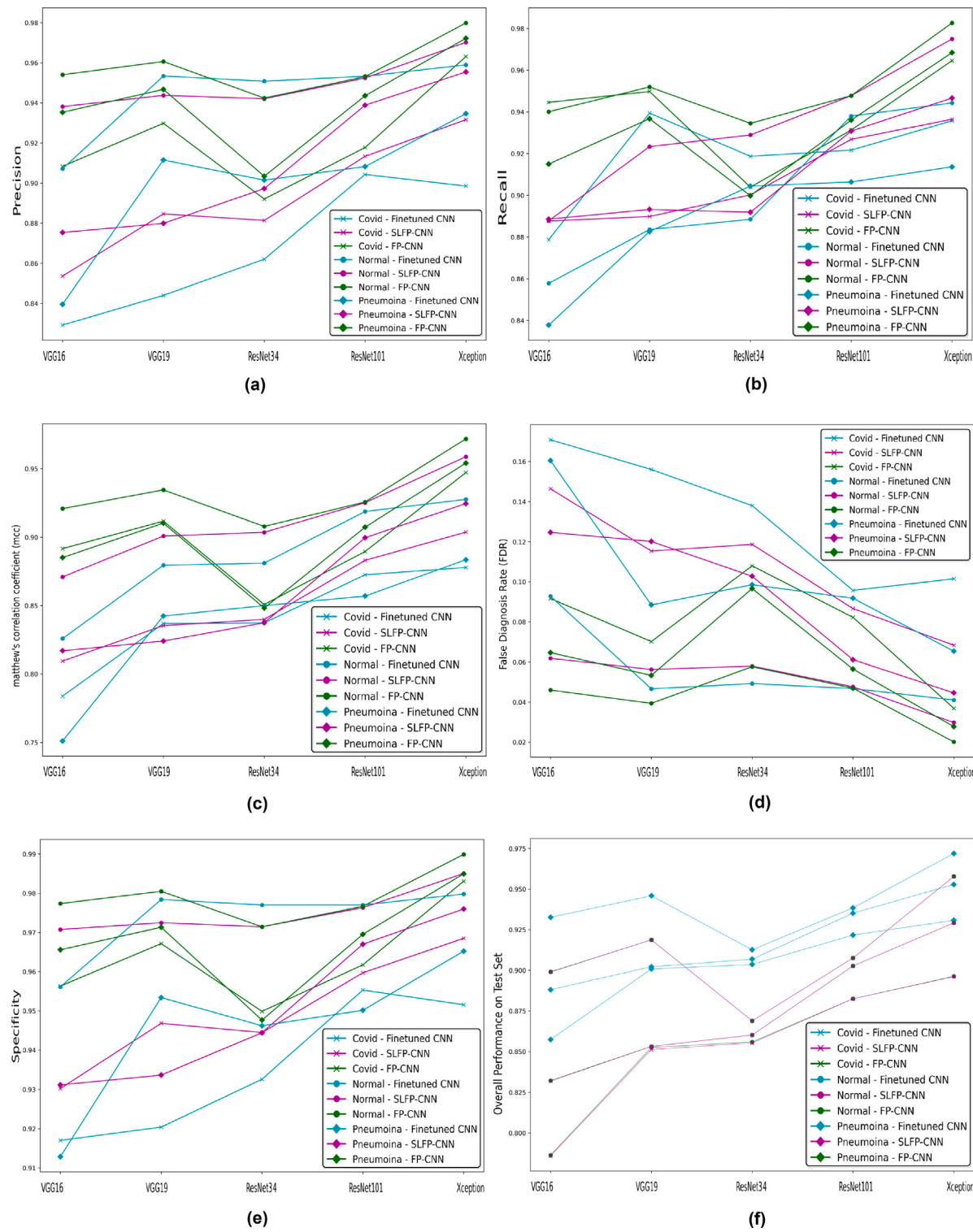


Fig. 16. Comparative performance analysis of different models on three strategies.

projected classes. In the visualization, a few pixels play a crucial part in classification. Different colors indicate pixels' Shapley values.

5. Discussion

In this study, we utilized a fuzzy pooling-based Xception model for lung disease diagnosis. We evaluated the performance of our model on

a dataset of US images and compared it to the traditional Xception model with max pooling. Our results showed that the fuzzy pooling-based Xception model achieved improved performance for pneumonia and COVID-19 classification. Fuzzy pooling uses multiple membership functions to create and find the pooled, unlike max-pooling. It is used to increase the robustness of CNNs by allowing the network to consider multiple pooling options simultaneously. In contrast, traditional

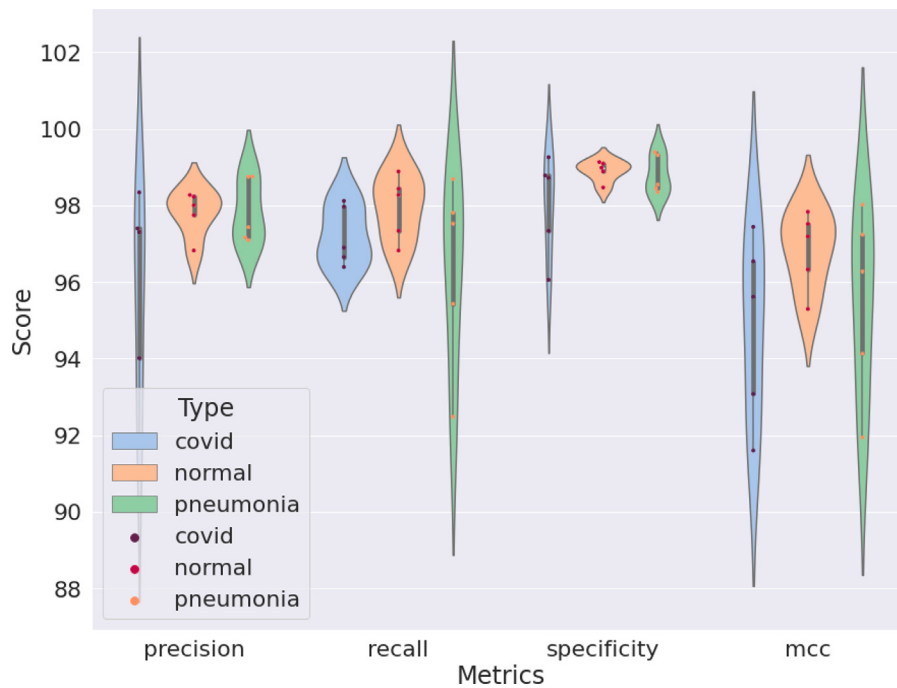


Fig. 17. Performance of five-fold cross-validation using fuzzy-based pooling layers.

Table 6
Performance comparison of the proposed method with existing works in literature.

Method	Dataset	Technique	Accuracy
Diaz-Escobar et al. [31]	COVID-19(1283), Pneumonia(731), Disease-free(1312)	InceptionV3 CNN model	89.1%
Born et al. [33]	COVID-19(654), Pneumonia(277), Disease-free(172)	POCOVID-net	89%
Muhammad and Hossain [34]	COVID-19(1673), Pneumonia(1007), Disease-free(951)	Multilayer feature fusion-based CNN model	92.5%
Barros et al. [39]	COVID-19(69), Pneumonia(50), Disease-free(66)	Optuna framework-based parameters optimized hybrid CNN-LSTM model	93%
Hou et al. [40]	B-line(1150), A-line(740), consolidation(910)	Saab Subspace network (Proposed fancy DL model)	96%
Bhosale and Patnaik [60]	COVID-19 (650), Pneumonia (650), Disease-free (650)	GNN and CNN	97.26%
Proposed method	COVID-19 (1353), Pneumonia (1517), Disease-free (1435)	Fuzzy-pooling based Xception model	97.2%

pooling techniques, such as max pooling, only one pooling option at a time. Also, fuzzy pooling is more robust against image degradation, such as noise or poor image quality, by providing a more robust feature representation.

This study applied image enhancement techniques such as isotropic diffusion and CLAHE. The isotropic diffusion method ensures improved image denoising and preserves edges and fine details in the image while smoothing out noises. This made it easier for feature extractors such as CNN models to identify the structures and features in ultrasound images. Also, isotropic diffusion is effective against varying levels of noise in ultrasound images. The inclusion of CLAHE reduced the halo artifacts of homogeneous regions of US images and enhanced the contrast of the image with improved diagnostic accuracy. The combination of isotropic diffusion and CLAHE works adaptively on images making it better suited for US images.

Max pooling is a simple technique that involves taking the maximum value from a small region (e.g. 2×2 pixels) in the feature map. This reduces the spatial dimensionality by a factor of 2 while maintaining the most important features. The complexity of max pooling is $O(N)$, where N is the number of elements in the feature map. However, fuzzy pooling uses a set of membership functions for pooling more representative features. The complexity of fuzzy pooling depends on the number of membership functions. Thus, fuzzy pooling is more computationally complex than max pooling; however, fuzzy pooling is robust to image degradation. Thus, we need to choose between the computational efficiency of max pooling and the performance of fuzzy pooling. Considering the results of fuzzy pooling compared to

its computational complexity, it is worth using fuzzy pooling for lung ultrasound image classification.

Our proposed method has better classification accuracy than existing state-of-the-art methods for Lung US image classification. The designed method has utilized the advantages of image enhancement techniques and the fuzzy pooling method. The proposed method had improved noise reduction with better feature representation and was adaptive to different image acquisition techniques with improved accuracy.

6. Conclusion

Ultrasound imaging is a non-invasive imaging modality that can play a significant role in areas lacking highly advanced medical facilities. The low cost and availability of ultrasound machines can be effective for pandemic scenarios. However, ultrasound images are not primarily used in lung-related diagnoses. This study designed a diagnostic methodology with evidence of the diagnostic decision for lung-related diseases (covid and pneumonia) diagnosis. The developed method of our research performed significantly well in classifying ultrasound images. The fuzzy pooling layer of the network architecture helped to extract useful features. The comparative analysis of different state-of-the-art architectures with three modalities of training, specifically fine-tuned models without fuzzy pooling, single-layer fuzzy pooling, and all pooling layers with fuzzy pooling, showed the effectiveness of the fuzzy pooling algorithm. The explainable technique of SHAP illustrated the contribution of each pixel to the predicted output.

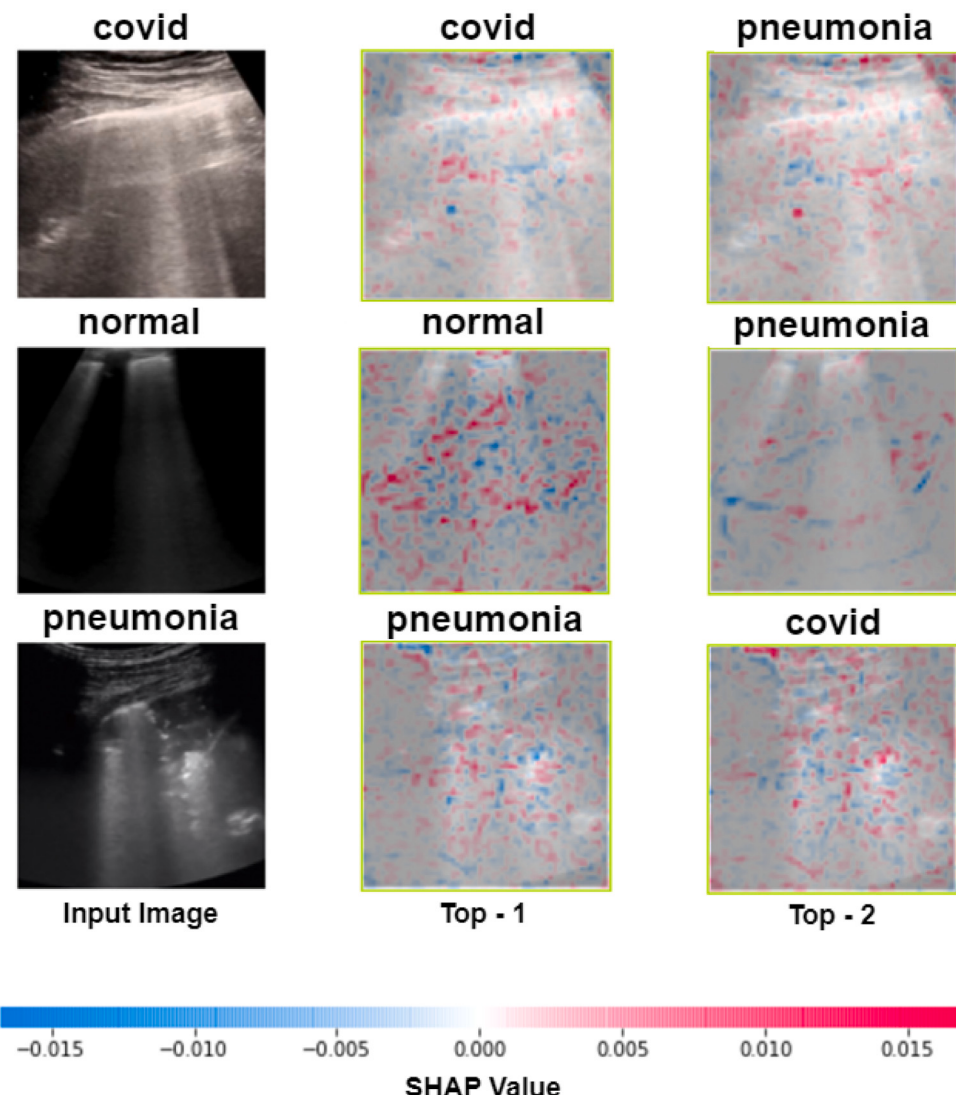


Fig. 18. Pixel-wise Shapley value contribution of top two predictions of the LUS images.

In addition, the developed method achieved better results than existing state-of-the-art methods. However, one limitation of this research is that the proposed method has not denoted the severity of the disease as part of its explainability. In the future, the severity of the diagnosed disease could be studied to find the stage of the disease for better meditative care of patients. Our proposed framework could also be applicable to diagnosing other lung-related diseases using ultrasound images.

Declaration of competing interest

The authors declare that they have no conflicts of interest regarding publishing the paper.

Acknowledgments

The authors extend their appreciation to the King Salman Center for Disability Research for funding this work through Research Group number KSRG-2023-253.

Appendix A. List of abbreviations

Acronyms

AI Artificial intelligence.

CLAHE Contrast Limited Adaptive Histogram Equalization.

CNN Convolution Neural Network.

DL Deep learning.

FP-CNN Fuzzy pooling-based convolutional neural network.

IoT Internet of Things.

LUS Lung ultrasound.

ML Machine learning.

ReLU Rectified Linear Unit.

RT-PCR Reverse transcription polymerase chain reaction.

SARS-CoV-2 Severe acute respiratory syndrome coronavirus

SHAP SHapley Additive Explanation.

XAI Explainable AI.

Appendix B. List of performance calculating formulae

$$i^{\text{th}} \text{ class Precision}, \quad \text{Precision}_{C_i} = \frac{TP_{C_i}}{TP_{C_i} + \sum_{j=1}^{i-1} FP_{C_j C_i} + \sum_{j=i+1}^n FP_{C_j C_i}}$$

$$i^{\text{th}} \text{ class Recall}, \quad \text{Recall}_{C_i} = \frac{TP_{C_i}}{TP_{C_i} + \sum_{j=1}^{i-1} FN_{C_i C_j} + \sum_{j=i+1}^n FN_{C_i C_j}}$$

$$i^{\text{th}} \text{ class Specificity}, \quad \text{Specificity}_{C_i} = \frac{\sum TN_{C_i}}{\sum TN_{C_i} + \sum_{j=1}^{i-1} FP_{C_j C_i} + \sum_{j=i+1}^n FP_{C_j C_i}}$$

$$\text{Accuracy} = \frac{TP + TN}{TP + TN + FP + FN}$$

$$\text{Precision} = \frac{TP}{TP + FP}$$

$$\text{Recall} = \frac{TP}{TP + FN}$$

$$\text{Specificity} = \frac{TN}{TN + FP}$$

$$\text{False Positive Rate (FPR)}, \quad FPR = \frac{FP}{TN + FP}$$

Matthews Correlation Coefficient (MCC),

$$MCC = \frac{TP \times TN - FP \times FN}{\sqrt{(TP + FP)(TP + FN)(TN + FP)(TN + FN)}}$$

References

- [1] World health organization, 2022, <https://covid19.who.int/> [Last Access: 23 2022].
- [2] T. Liang, Handbook of COVID-19 prevention and treatment. The first affiliated hospital, Zhejiang University School of medicine, Compiled Accord. Clin. Exp. (2020) 68.
- [3] S.H. Safiabadi Tali, J.J. LeBlanc, Z. Sadig, O.D. Oyewunmi, C. Camargo, B. Nikpour ..., S. Jahanshahi-Anbuhi, Tools and techniques for severe acute respiratory syndrome coronavirus 2 (SARS-CoV-2)/COVID-19 detection, Clin. Microbiol. Rev. 34 (3) (2021) e00228-e00220.
- [4] M. Teymour, S. Mollazadeh, H. Mortazavi, Z.N. Ghale-Noie, V. Keyvani, F. Aghababaei ., H. Mirzaei, Recent advances and challenges of RT-PCR tests for the diagnosis of COVID-19, Pathol.-Res. Pract. 221 (2021) 153443.
- [5] E. Showkatian, M. Salehi, H. Ghaffari, R. Reiazi, N. Sadighi, Deep learning-based automatic detection of tuberculosis disease in chest X-ray images, Polish J. Radiol. 87 (1) (2022) 118–124.
- [6] S.I. Nafisah, G. Muhammad, Tuberculosis detection in chest radiograph using convolutional neural network architecture and explainable artificial intelligence, Neural Comput. Appl. (2022) 1–21.
- [7] R. Mostafiz, M.S. Uddin, I. Jabin, M.M. Hossain, M.M. Rahman, Automatic brain tumor detection from MRI using curvellet transform and neural features, Int. J. Ambient Comput. Intell. (IJACI) 13 (1) (2022) 1–18.
- [8] J. Amin, M. Sharif, M. Raza, T. Saba, M.A. Anjum, Brain tumor detection using statistical and machine learning method, Comput. Methods Programs Biomed. 177 (2019) 69–79.
- [9] M.M. Hasan, M. Asaduzzaman, M.M. Rahman, M.S. Hossain, K. Andersson, D3mciad: data-driven diagnosis of mild cognitive impairment utilizing syntactic images generation and neural nets, in: Brain Informatics: 14th International Conference, BI 2021, Virtual Event, September (2021) 17–19, Proceedings, Vol. 14, Springer International Publishing, 2021, pp. 366–377.
- [10] X. Wang, Z. Li, H. Kang, Y. Huang, D. Gai, Medical image segmentation using PCNN based on multi-feature grey wolf optimizer bionic algorithm, J. Bionic Eng. 18 (2021) 711–720.
- [11] F. Uslu, A.A. Bharath, TMS-Net: A segmentation network coupled with a runtime quality control method for robust cardiac image segmentation, Comput. Biol. Med. 152 (2023) 106422.
- [12] Q. Han, H. Wang, M. Hou, T. Weng, Y. Pei, Z. Li ., Z. Qiu, HWA-SegNet: Multi-channel skin lesion image segmentation network with hierarchical analysis and weight adjustment, Comput. Biol. Med. 152 (2023) 106343.
- [13] J. Sang, M.S. Alam, H. Xiang, Automated detection and classification for early stage lung cancer on CT images using deep learning, in: Pattern Recognition and Tracking XXX, Vol. 10995, SPIE, 2019, pp. 200–207.
- [14] M.A. Kadampur, S. Al Riyaae, Skin cancer detection: Applying a deep learning based model driven architecture in the cloud for classifying dermal cell images, Inform. Med. Unlocked 18 (2020) 100282.
- [15] E. Hussain, M. Hasan, M.A. Rahman, I. Lee, T. Tamanna, M.Z. Parvez, CoroDet: A deep learning based classification for COVID-19 detection using chest X-ray images, Chaos Solitons Fractals 142 (2021) 110495.
- [16] R. Mostafiz, M.S. Uddin, K.M.M. Uddin, M.M. Rahman, COVID-19 along with other chest infection diagnoses using faster R-CNN and generative adversarial network, ACM Trans. Spat. Algorithms Syst. 8 (3) (2022) 1–21.
- [17] N. Habib, MM. Rahman, Diagnosis of corona diseases from associated genes and X-ray images using machine learning algorithms and deep CNN, Inform. Med. Unlocked 24 (2021) 100621.
- [18] M. Ahsan, M. Based, J. Haider, M. Kowalski, COVID-19 detection from chest X-ray images using feature fusion and deep learning, Sensors 21 (4) (2021) 1480.
- [19] T.B. Chandra, K. Verma, B.K. Singh, D. Jain, S.S. Netam, Coronavirus disease (COVID-19) detection in chest X-ray images using majority voting based classifier ensemble, Expert Syst. Appl. 165 (2021) 113909.
- [20] D.A. Zebari, A.M. Abdulazeez, D.Q. Zeebaree, M.S. Salih, A fusion scheme of texture features for COVID-19 detection of CT scan images, in: 2020 International Conference on Advanced Science and Engineering (ICOASE), IEEE, 2020, pp. 1–6.
- [21] S. Ahuja, B.K. Panigrahi, N. Dey, V. Rajnikanth, T.K. Gandhi, Deep transfer learning-based automated detection of COVID-19 from lung CT scan slices, Appl. Intell. 51 (1) (2021) 571–585.
- [22] P. Silva, E. Luz, G. Silva, G. Moreira, R. Silva, D. Lucio, D. Menotti, COVID-19 detection in CT images with deep learning: A voting-based scheme and cross-datasets analysis, Inform. Med. Unlocked 20 (2020) 100427.
- [23] H. Panwar, P.K. Gupta, M.K. Siddiqui, R. Morales-Menendez, P. Bhardwaj, V. Singh, A deep learning and grad-CAM based color visualization approach for fast detection of COVID-19 cases using chest X-ray and CT-scan images, Chaos Solitons Fractals 140 (2020) 110190.
- [24] K. Purohit, A. Kesarwani, D.Ranjan, Kisku, M. Dalui, Covid-19 detection on chest x-ray and ct scan images using multi-image augmented deep learning model, in: Proceedings of the Seventh International Conference on Mathematics and Computing, Springer, Singapore, 2022, pp. 395–413.
- [25] M.J. Horry, S. Chakraborty, M. Paul, A. Ulhaq, B. Pradhan, M. Saha, N. Shukla, COVID-19 detection through transfer learning using multimodal imaging data, Ieee Access 8 (2020) 149808-149824.
- [26] V. Shah, R. Keniya, A. Shridharani, M. Punjabi, J. Shah, N. Mehendale, Diagnosis of COVID-19 using CT scan images and deep learning techniques, Emerg. Radiol. 28 (3) (2021) 497–505.
- [27] V. Hartwig, G. Giovannetti, N. Vanello, M. Lombardi, L. Landini, S. Simi, Biological effects and safety in magnetic resonance imaging: a review, Int. J. Environ. Res. Public Health 6 (6) (2009) 1778–1798.
- [28] S.M. Bierig, A. Jones, Accuracy and cost comparison of ultrasound versus alternative imaging modalities, including CT, MR, PET, and angiography, J. Diagn. Med. Sonogr. 25 (3) (2009) 138–144.
- [29] M.A. Talukder, M.M. Islam, M.A. Uddin, A. Akhter, K.F. Hasan, M.A. Moni, Machine learning-based lung and colon cancer detection using deep feature extraction and ensemble learning, Expert Syst. Appl. 205 (2022) 117695.
- [30] N. Faruqui, M.A. Yousuf, M. Whaiduzzaman, A.K.M. Azad, A. Barros, M.A. Moni, LungNet: A hybrid deep-CNN model for lung cancer diagnosis using CT and wearable sensor-based medical IoT data, Comput. Biol. Med. 139 (2021) 104961.
- [31] J. Diaz-Escobar, N.E. Ordóñez Guillén, S. Villarreal-Reyes, A. Galaviz-Mosqueda, V. Kober, R. Rivera-Rodriguez, J.E. Lozano Rízquez, Deep-learning based detection of COVID-19 using lung ultrasound imagery, PLoS One 16 (8) (2021) e0255886.
- [32] O. Akter, M.A. Moni, M.M. Islam, J.M. Quinn, A.H.M. Kamal, Lung cancer detection using enhanced segmentation accuracy, Appl. Intell. 51 (2021) 3391–3404.
- [33] J. Born, N. Wiedemann, M. Cossio, C. Buhre, G. Brändle, K. Leidermann ., K. Borgwardt, Accelerating detection of lung pathologies with explainable ultrasound image analysis, Appl. Sci. 11 (2) (2021) 672.
- [34] G. Muhammad, M.S. Hossain, COVID-19 and non-COVID-19 classification using multi-layers fusion from lung ultrasound images, Inf. Fusion 72 (2021) 80–88.
- [35] M.K.U. Ahmed, M.M. Islam, M.A. Uddin, A. Akhter, U.K. Acharjee, B.K. Paul, M.A. Moni, DTLCx: An improved ResNet architecture to classify normal and conventional pneumonia cases from COVID-19 instances with grad-CAM-based superimposed visualization utilizing chest X-ray images, Diagnostics 13 (3) (2023) 551.
- [36] K.U. Ahmed, M. Islam, A. Uddin, A. Akhter, B.K. Paul, M.A. Yousuf ., M.A. Moni, A deep learning approach using effective preprocessing techniques to detect COVID-19 from chest CT-scan and X-ray images, Comput. Biol. Med. 139 (2021) 105014.
- [37] M.K. Hasan, M.T. Jawad, K.N.I. Hasan, S.B. Partha, M.M. Al Masba, S. Saha, M.A. Moni, COVID-19 identification from volumetric chest CT scans using a progressively resized 3D-CNN incorporating segmentation, augmentation, and class-rebalancing, Inform. Med. Unlocked 26 (2021) 100709.
- [38] K.M.M. Uddin, S.K. Dey, H.M.H. Babu, R. Mostafiz, S. Uddin, W. Shoombuatong, M.A. Moni, Feature fusion based VGGFusionNet model to detect COVID-19 patients utilizing computed tomography scan images, Sci. Rep. 12 (1) (2022) 21796.
- [39] B. Barros, P. Lacerda, C. Albuquerque, A. Conci, Pulmonary COVID-19: learning spatiotemporal features combining CNN and LSTM networks for lung ultrasound video classification, Sensors 21 (16) (2021) 5486.
- [40] D. Hou, R. Hou, J. Hou, Interpretable saab subspace network for COVID-19 lung ultrasound screening, in: 2020 11th IEEE Annual Ubiquitous Computing, Electronics & Mobile Communication Conference (UEMCON), IEEE, 2020, pp. 0393–0398.
- [41] Y.H. Bhosale, K.S. Patnaik, IoT deployable lightweight deep learning application for COVID-19 detection with lung diseases using RaspberryPi, in: 2022 International Conference on IoT and Blockchain Technology (ICIBT), IEEE, 2022, pp. 1–6.

- [42] Y.H. Bhosale, S. Zanwar, Z. Ahmed, M. Nakrani, D. Bhuyar, U. Shinde, Deep convolutional neural network based Covid-19 classification from radiology X-ray images for IoT enabled devices, in: 2022 8th International Conference on Advanced Computing and Communication Systems (ICACCS), Vol. 1, IEEE, 2022, pp. 1398–1402.
- [43] B. Pal, D. Gupta, M. Rashed-Al-Mahfuz, S.A. Alyami, M.A. Moni, Vulnerability in deep transfer learning models to adversarial fast gradient sign attack for covid-19 prediction from chest radiography images, *Appl. Sci.* 11 (9) (2021) 4233.
- [44] Y.H. Bhosale, K.S. Patnaik, Application of deep learning techniques in diagnosis of covid-19 (coronavirus): a systematic review, *Neural Process. Lett.* (2022) 1–53.
- [45] Y.H. Bhosale, K.S. Patnaik, PulDi-COVID: Chronic obstructive pulmonary (lung) diseases with COVID-19 classification using ensemble deep convolutional neural network from chest X-ray images to minimize severity and mortality rates, *Biomed. Signal Process. Control* 81 (2023) 104445.
- [46] Y.H. Bhosale, P. Singh, K.S. Patnaik, COVID-19 and associated lung disease classification using deep learning, in: International Conference on Innovative Computing and Communications: Proceedings of ICICC 2022, Vol. 3, Springer Nature Singapore, Singapore, 2022, pp. 283–295.
- [47] Y.H. Bhosale, K.S. Patnaik, ECG-CCNet: Cardiovascular (cardiac) and COVID-19 disease classification using deep convolutional neural network learning pipeline approaches from electrocardiography (ECG)-A study, in: 2022 IEEE Silchar Subsection Conference (SILCON), IEEE, 2022, pp. 1–6.
- [48] A. Qi, D. Zhao, F. Yu, A.A. Heidari, Z. Wu, Z. Cai, M. Chen, Directional mutation and crossover boosted ant colony optimization with application to COVID-19 X-ray image segmentation, *Comput. Biol. Med.* 148 (2022) 105810.
- [49] Y. Han, W. Chen, A.A. Heidari, H. Chen, Multi-verse optimizer with rosenbrock and diffusion mechanisms for multilevel threshold image segmentation from COVID-19 chest X-ray images, *J. Bionic Eng.* 20 (3) (2023) 1198–1262.
- [50] M.A. Moid, M.A. Chaurasia, Transfer learning-based plant disease detection and diagnosis system using Xception, in: 2021 Fifth International Conference on I-SMAC (IoT in Social, Mobile, Analytics and Cloud)(I-SMAC), IEEE, 2021, pp. 1–5.
- [51] D. Gunning, M. Stefk, J. Choi, T. Miller, S. Stumpf, G.Z. Yang, XAI—Explainable artificial intelligence, *Sci. Robot.* 4 (37) (2019) 7120.
- [52] D. Doran, S. Schulz, T.R. Besold, What does explainable AI really mean? A new conceptualization of perspectives, 2017, arXiv preprint [arXiv:1710.00794](https://arxiv.org/abs/1710.00794).
- [53] J. Born, N. Wiedemann, M. Cossio, et al., L2 accelerating COVID-19 differential diagnosis with explainable ultrasound image analysis: an AI tool, 2021, pp. A230–A231, 2021.
- [54] P. Perona, J. Malik, Scale-space and edge detection using anisotropic diffusion, *IEEE Trans. Pattern Anal. Mach. Intell.* 12 (7) (1990) 629–639.
- [55] S.M. Pizer, Contrast-limited adaptive histogram equalization: Speed and effectiveness stephen m. pizer, r. eugene johnston, james p. ericksen, bonnie c. yankaskas, keith e. muller medical image display research group, in: Proceedings of the First Conference on Visualization in Biomedical Computing, Vol. 337, Atlanta, Georgia, 1990, p. 2.
- [56] D.E. Diamantis, D.K. Iakovidis, Fuzzy pooling, *IEEE Trans. Fuzzy Syst.* 29 (11) (2020) 3481–3488.
- [57] A. Singh, S. Sengupta, V. Lakshminarayanan, Explainable deep learning models in medical image analysis, *J. Imaging* 6 (6) (2020) 52.
- [58] S.M. Lundberg, S.I. Lee, A unified approach to interpreting model predictions, *Adv. Neural Inf. Process. Syst.* (2017) 30.
- [59] P. Gavrikov, Visualkeras, GitHub, 2022, [Online]. Available: <https://github.com/paulgavrikov/visualkeras> Accessed July 18, 2023.
- [60] Y.H. Bhosale, K.S. Patnaik, Graph and capsule convolutional neural network based classification of Lung Cancer, Pneumonia, COVID-19 using lung CT and ultrasound radiography imaging, in: 2022 8th International Conference on Signal Processing and Communication (ICSC), IEEE, 2022, pp. 381–387.